Physics-Inspired Inverse Measurement of Position, Depth, and Force Using Conductive Polymer Tactile Instrumentation

Sarun Phibanchon, Suchanya Jankong, Nililla Nisoh, Pornkamon Nalakarn, Saree Phongphanphanee, Nanthiya Hansupalak, Panithi Wiroonpochit, Sasitorn Srisawadi, and Jirasak Wong-Ekkabut

***Abstract*—Recovering mechanical loading parameters from a small number of boundary electrode signals is a long-standing instrumentation problem for conductive polymer tactile devices. Inverse tactile measurement using boundary-mounted electrodes is fundamentally challenging due to the nonlinear, coupled, and partially nonidentifiable relationship between electrical resistance patterns and applied mechanical loading. In conductive polymer sensors operating near the percolation threshold, tunneling effects, nonuniform strain fields, and contact-mechanics-induced coupling further complicate the recovery of spatial position, indentation depth, and applied force. This work presents a physics-inspired inverse measurement framework for simultaneous estimation of lateral position (x, y), indentation depth z, and applied pressure P from twelve boundary resistance channels. Of particular relevance to instrumentation is the constraint that all mechanical information must be inferred indirectly, from boundary electrical measurements alone, without access to distributed internal sensing. Physically inspired feature operators derived from percolation and tunneling behavior are paired with validation-guided selection among candidate regressors. For the present dataset, this procedure selects the extra trees (ETs) regressor as the final predictor; the residual neural network (ResNN) is evaluated only as a comparative neural baseline. Using a CNC-controlled indentation platform and a 5 × 5 cm conductive natural-rubber sensor, the selected predictor achieves an overall inverse-estimation accuracy of $R^2_{\text{overall}} = 0.9103$ on the held-out test set. Parameter-wise test scores reach $R^2 = 0.9466$ for x, 0.9762 for y, 0.8516 for z, and 0.8670 for P. Physics-inspired feature operators remain important for prediction quality, and the uncertainty analysis reveals clear links between prediction confidence and intrinsic measurement ambiguity arising from electrode geometry and parameter coupling, providing physically interpretable confidence measures for tactile instrumentation.**

***Index Terms*—Conductive polymers, Inverse measurement, multiparameter estimation, physics-inspired feature engineering, tactile instrumentation, uncertainty quantification.**

I. Introduction

SOFT and flexible tactile sensors have become increasingly important across multiple domains, ranging from healthcare monitoring and wearable electronics to human–machine interfaces and robotic manipulation. Their mechanical compliance and rich deformation-dependent electromechanical behavior offer distinct advantages over conventional rigid sensors, particularly in applications requiring conformability and adaptability [1], [2].

Soft elastomers such as polydimethylsiloxane (PDMS), Ecoflex, polyurethane, silicone rubber, and natural rubber (NR) provide the mechanical foundation for flexible devices. However, these materials alone typically lack sufficient electrical responsiveness under mechanical loading. Material modification through the incorporation of conductive fillers—such as carbon black, graphite, graphene, carbon nanotubes, or metallic nanoparticles—enables electrical signal changes in response to deformation, creating piezoresistive sensing capabilities [3], [4], [5], [6], [7], [8], [9], [10], [11], [12], [13].

Among various elastomer matrices, NR stands out as an environmentally sustainable option derived from renewable resources [14]. Recent studies have shown that NR composites with conductive fillers demonstrate exceptional mechanical performance, cyclic durability, and ultrahigh sensitivity [15], [16], [17], [18], [19], [20]. For instance, bilayer thin-film sensors composed of nonconductive prevulcanized NR substrates and conductive carbon-black layers have achieved gauge fac-

Received 15 April 2026; revised 23 May 2026; accepted 25 May 2026. Date of publication 8 June 2026; date of current version 18 June 2026. This work was supported by the National Science Research and Innovation fund (NSRF) via the Program Management Unit for Human Resources and Institutional Development Research and Innovation (PMUB) under Grant B42G670041. The Associate Editor coordinating the review process was Dr. Thiago Destri Cabral. *(Corresponding author: Jirasak Wong-Ekkabut.)*

Sarun Phibanchon is with the Department of Innovation and Educational Technology, Faculty of Education, Burapha University, Chonburi 20131, Thailand, and also with the Computational Biomodelling Laboratory for Agricultural Science and Technology (CBLAST), Faculty of Science, Kasetsart University, Bangkok 10900, Thailand.

Suchanya Jankong and Nililla Nisoh are with CBLAST, Faculty of Science, and the Department of Physics, Kasetsart University, Bangkok 10900, Thailand.

Pornkamon Nalakarn is with CBLAST, Faculty of Science, Kasetsart University, Bangkok 10900, Thailand, and also with the Department of Physics, Faculty of Science and Technology, Thammasat University, Pathum Thani 12120, Thailand.

Saree Phongphanphanee is with CBLAST, Faculty of Science, the Department of Materials Science, and the Specialized Center of Rubber and Polymer Materials for Agriculture and Industry, Kasetsart University, Bangkok 10900, Thailand.

Nanthiya Hansupalak is with the Department of Chemical Engineering, Faculty of Engineering, and the Specialized Center of Rubber and Polymer Materials for Agriculture and Industry, Faculty of Science, Kasetsart University, Bangkok 10900, Thailand.

Panithi Wiroonpochit and Sasitorn Srisawadi are with the National Metal and Materials Technology Center (MTEC), National Science and Technology Development Agency (NSTDA), Pathum Thani 12120, Thailand.

Jirasak Wong-Ekkabut is with CBLAST, Faculty of Science, the Department of Physics, and the Specialized Center of Rubber and Polymer Materials for Agriculture and Industry, Kasetsart University, Bangkok 10900, Thailand (e-mail: jirasak.w@ku.th).

Digital Object Identifier 10.1109/TIM.2026.3701097

tors exceeding 10 000 with stable operation over more than 5000 cycles [12]. The bilayer architecture effectively separates mechanical support from electrical conduction, reducing the stiffness-sensitivity tradeoff that often limits single-phase composites.

Despite these material advances, most existing conductive composite sensors operate primarily in 1-D sensing modes, where electrical conductivity changes as a direct response to uniaxial stretching. While such sensors effectively capture strain or elongation, they provide only a single scalar measurement. Achieving true 2-D spatial sensing capability—such as mapping pressure distributions or generating spatial potential profiles—typically requires integrating sensor arrays with additional circuitry, multiplexing components, and patterned electrode layouts, significantly increasing system complexity [23], [18], [19].

Here, we develop a 2-D pressure sensor from conductive elastomer by exploiting electrical conduction through a percolated conductive network within the elastomeric sheet. The critical challenge lies in solving the *inverse problem* of estimating multidimensional mechanical loading parameters—spatial position, indentation depth, and applied force—directly from electrical resistance signals. This inverse mapping exhibits high nonlinearity due to quantum tunneling effects [20], nonuniform strain fields, hysteresis, and percolation dynamics. Traditional forward physics models require extensive calibration and computationally expensive finite element simulations.

Machine learning offers an alternative data-driven approach capable of learning these complex mappings. Recent work has demonstrated the effectiveness of deep learning for piezoresistive sensor applications, including long-term performance prediction [21], multimodal tactile perception [22], and electrical impedance tomography [23]. However, existing studies generally focus on single-parameter prediction, discrete contact classification, or lack comprehensive uncertainty quantification [24], [25].

This study proposes a physics-inspired empirical learning framework for prediction (x, y, z, P) from 12-channel resistive measurements. The approach combines physically motivated feature construction derived from percolation and tunneling considerations with validation-guided comparison of candidate regressors, including residual neural network (ResNN), random forest (RF), and extra trees (ETs) models. The final predictor is selected from validation performance rather than fixed a priori, while uncertainty is estimated from model spread and residual variance. This terminology is used deliberately: the present method does not impose explicit governing equations, contact-mechanics constraints, or a mechanistic forward model during training. Here, x and y denote the lateral position, z is the depth of the indentation and P is the applied pressure.

Contributions: The principal contributions of this work are: 1) a unified inverse measurement formulation that simultaneously recovers lateral position, indentation depth, and applied pressure from twelve boundary resistance signals, without decomposing the problem into sequential single-parameter subtasks; 2) physics-inspired feature operators motivated by percolation theory, tunneling behavior, and electrode coupling; 3) a validation-guided model comparison showing that the ETs regressor, rather than the tested neural baseline, is the appropriate final predictor for the present dataset; and 4) an uncertainty quantification scheme explicitly linked to identifiability limitations of the electrode geometry.

The methodology is implemented in Python, producing evaluation and visualization figures throughout this manuscript. This approach aligns with emerging trends in smart tactile sensing systems that combine advanced materials, multimodal perception, and intelligent data processing [26], [27]. From an instrumentation perspective, the central challenge is therefore not only achieving high prediction accuracy, but determining which mechanical parameters are physically observable from boundary-mounted electrical measurements and under what operating conditions such inference remains reliable. To address this question in a systematic manner, the inverse estimation problem and the experimental measurement system are formalized in Section II.

The remainder of this article is organized as follows. Section II states the inverse problem and describes the fabricated sensor, electrode layout, and data acquisition procedure. Section III examines identifiability and parameter coupling inherent to the boundary-electrode configuration. Section IV develops the validation-guided learning methodology, covering feature engineering, candidate regressors, model selection, and uncertainty quantification. Experimental results are presented in Section V, followed by extended analysis and discussion in Section VI. Section VII concludes.

II. Problem Formulation and Experimental Setup

A. Inverse Problem Statement

Given a 12-channel resistance vector

$$\mathbf{X} = [r_1, \ldots, r_{12}] \in \mathbb{R}^{12} \tag{1}$$

where r_i represents the resistance in channel i, our objective is to estimate the continuous mechanical loading vector

$$\mathbf{y} = \left[x, y, z, P\right] \in \mathbb{R}^4. \tag{2}$$

The inverse problem is formulated as

$$\mathbf{y} = g\left(\mathbf{X}\right) + \boldsymbol{\epsilon} \tag{3}$$

where $g(\cdot)$ represents an unknown nonlinear mapping and $\boldsymbol{\epsilon}$ models noise arising from material hysteresis, analog-to-digital converter (ADC), and strain-rate variations. The underlying mapping presents notable difficulties due to its nonuniqueness, strong nonlinearity, and intrinsic variable coupling. In practice, a single resistance pattern may correspond to more than one spatial configuration, tunneling and percolation effects introduce exponential variations in resistance, and pressure and depth are linked through contact mechanics. These characteristics necessitate a model with sufficient capacity, appropriate regularization, and reliable uncertainty estimation.

B. Material Fabrication

The conductive rubber specimen (Fig. 1) was fabricated by coating a NR blend, containing carbon-black fillers

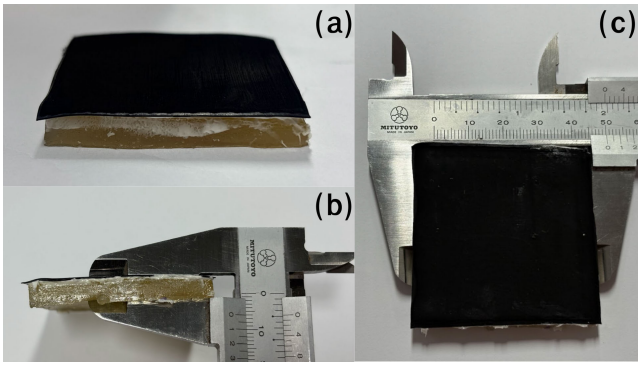

Fig. 1. Fabricated conductive rubber sample. (a) Overall sheet geometry. (b) Surface uniformity. (c) Caliper measurement confirming dimensions.

near the percolation threshold, onto a nonconductive sulfur-prevulcanized NR layer. Keawmaungkom et al. [12] This structure yielded strong piezoresistive behavior under compression. The conductive layer (CNR) was formulated using acetylene black (AB, AB50, particle size 30–50 nm) at 9 phr incorporated into a sulfur-prevulcanized NR (S-PVNR) latex matrix [12]. The nonconductive substrate (PVNR layer, 0.108 mm dry thickness) was coated first and partially dried at 60 °C for 1 min inside the coating machine; the CNR layer (0.125 mm dry thickness) was then applied directly onto the still-partially-wet PVNR surface to promote polymer chain interdiffusion and strong interfacial adhesion. The complete bilayer assembly was oven-dried at 70 °C for 1 h, yielding a total sensor film thickness of approximately 0.233 mm. The nonconductive substrate provides mechanical support and elasticity under repeated compression, while the CNR layer delivers the piezoresistive response. The resulting 0.35 mm thick conductive rubber sheet was incorporated on top of a pressure-responsive rubber gel designed to deform and recover under applied pressure. The final specimen dimensions were $5 \times 5\,\text{cm}^2$ with a total thickness of approximately 6 mm. A digital caliper was used to verify dimensional uniformity.

C. Twelve-Channel Resistive Sensor Layout

Twelve electrodes (R_1–R_{12}) were evenly distributed around the sample edges (Fig. 2). This configuration captures directional changes in conductive pathways during compression, enabling spatial inference from boundary electrode signals without requiring a complex internal sensor array. Three electrodes are placed on each of the four sides, giving symmetric perimeter coverage. Copper contacts were applied at each site and allowed to cure at room temperature for 24 h prior to any measurements. The choice of 12 electrodes reflects a practical balance: denser arrays improve spatial sensitivity but add hardware complexity and increase the number of channels that must be sampled and conditioned, while sparser layouts reduce identifiability—particularly near sensor boundaries where resistance gradients from opposing sides become difficult to distinguish. The consequences of this symmetric layout for positional degeneracy are discussed in detail in Section III.

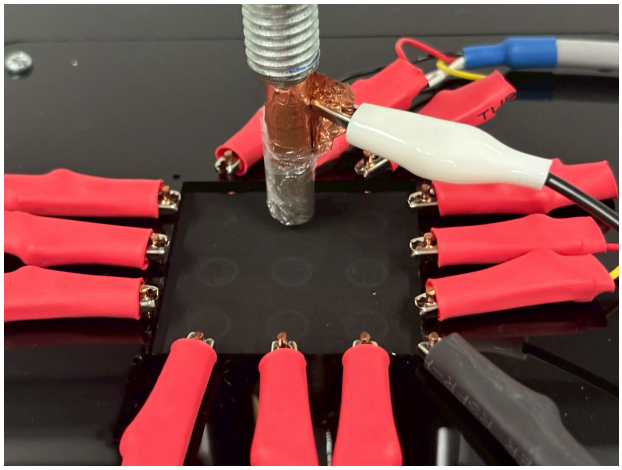

Fig. 2. Twelve-channel resistive sensor layout used for data acquisition.

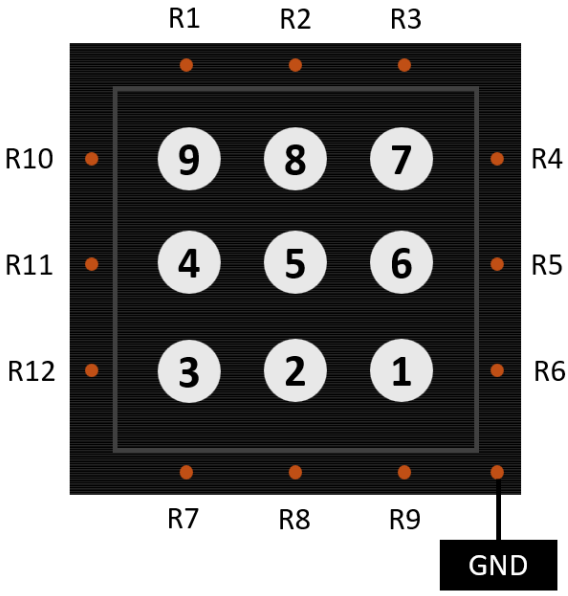

Fig. 3. Indentation grid showing nine pressing positions (P1–P9) distributed across the sensing area.

D. Pressing Positions

Indentation testing are performed at nine spatial locations distributed across the specimen, as shown in Fig. 3. A cylindrical probe with 7 mm diameter (area $A = \pi \times (3.5\,\text{mm})^2$) was used for all measurements.

E. Data Acquisition Protocol

Measurements were acquired using a CNC indentation stage coupled to a Raspberry Pi, which recorded the 12-channel resistance vector, probe coordinates (x, y, z), and load cell force synchronously at each compression step. At each of the nine spatial positions, the probe was driven into the specimen in uniform depth increments from 5 % to 50 % of total thickness, held for 5 s at each level to allow the signal to settle, then retracted; a 1 min recovery period followed before the next indentation cycle. The full procedure yielded more than

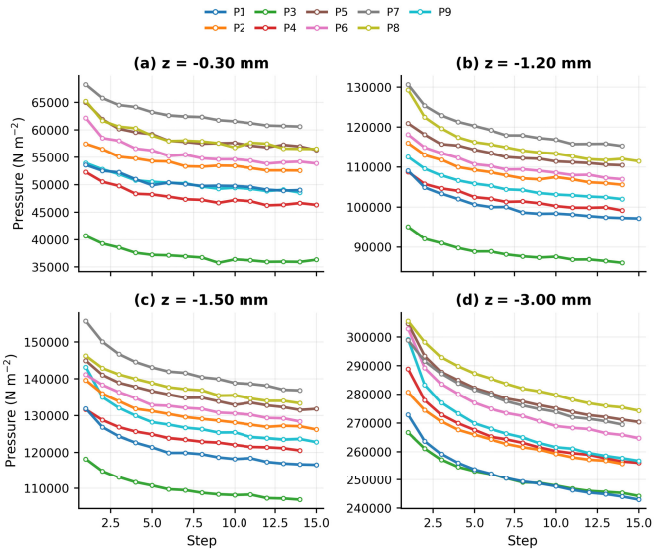

Fig. 4. Force-resistance response curves obtained through stepped indentation protocol with synchronized force sensing across all nine spatial positions (P1–P9). (a) Pressure measurements at 0.3 mm depth from surface showing initial contact response. (b) Pressure measurements at 0.9 mm depth from surface demonstrating intermediate compression behavior. (c) Pressure measurements at 1.2 mm depth from surface exhibiting enhanced piezoresistive coupling. (d) Pressure measurements at 3.0 mm depth from surface revealing maximum compression characteristics. The depth-dependent force evolution across all positions enables comprehensive multiparameter inverse estimation.

450 steady-state measurements covering the sensor's operating range.

Resistance across all 12 channels was sampled simultaneously through a multiplexed ADC operating at 100 Hz. To suppress transient effects, each reported measurement represents the mean of 50 samples acquired during the final 0.5 s of the 5 s hold period at each depth increment. Raw ADC values were converted to resistance using a fixed reference voltage and series resistor divider, then subjected to 3-σ outlier rejection applied channel-by-channel, followed by min-max normalization over the full dataset. Repeated measurements at identical positions yielded a coefficient of variation below 2.3 % across all channels, indicating stable sensor response under the controlled conditions. Ambient temperature was held at 25 °C ± 1 °C throughout.

F. Observed Force-Resistance Characteristics

The stepped indentation protocol produced a dataset that illustrates the nonlinear character of the piezoresistive response across the full spatial and depth range. At each position, force and resistance were recorded simultaneously as the probe moved from 0.3 to 3.0 mm depth in discrete increments, with each point on the horizontal axis of Fig. 4 representing the steady-state value at that depth. Representative curves across all nine positions are shown; the position-to-position variation is substantial and motivates the machine-learning approach.

Corner positions (P1, P3, P7, P9) show consistently lower piezoresistive sensitivity than central positions, as the boundary electrode geometry restricts available current paths at the corners. The center position (P5) yields the widest dynamic range and the highest signal-to-noise ratio, consistent with the more uniform current distribution expected there. In all cases, resistance changes with depth in a nonlinear fashion that is qualitatively consistent with percolation and tunneling mechanisms.

III. Identifiability and Parameter Coupling

Although the experimental protocol provides a rich dataset spanning spatial position, indentation depth, and applied force, not all mechanical parameters are equally observable from boundary-mounted resistive measurements. Sensor geometry, electromechanical coupling, and material nonlinearity each impose constraints on what can be reliably inferred, and some of the resulting ambiguities are irreducible—they reflect physical limitations of the measurement configuration rather than shortcomings of the learning model. This section examines those limitations before the learning architecture is introduced.

A. Coupling Between Mechanical Parameters

The mechanical variables considered in this work—lateral position (x, y), indentation depth z, and applied pressure P—do not affect the electrical response independently. Instead, they are strongly coupled through both contact mechanics and conductive-network deformation. As indentation depth increases, the contact area between the probe and the sensor expands, which in turn modifies the force distribution and alters current pathways within the percolated network. Consequently, different combinations of (z, P) may produce resistance patterns that are difficult to distinguish based on boundary measurements alone.

This coupling is particularly pronounced at shallow indentation depths, where small changes in contact geometry can lead to relatively large variations in resistance. In this regime, depth and pressure are only weakly separable, and the inverse mapping becomes inherently ambiguous. We emphasize that this ambiguity is a physical property of the sensing mechanism rather than a limitation of the learning model itself.

Lateral position (x, y) is also subject to coupling effects imposed by the electrode layout. While asymmetric current redistribution enables spatial localization, electrode symmetry can introduce degeneracy, especially near corners and edges of the sensing area. As a result, multiple spatial locations may yield similar resistance gradients, limiting positional identifiability in those regions. The symmetric arrangement of three electrodes per side introduces reflection symmetry about both sensor centerlines, which has direct consequences for positional identifiability. A probe located at (x, y) and its mirror image at $(-x, y)$ can produce very similar boundary resistance patterns, since the induced current redistribution is nearly symmetric under that reflection. Disambiguation then relies on small asymmetries in the conductive network or minor differences in electrode contact resistance—effects that are real but not always sufficient to resolve the ambiguity reliably. The problem is most acute when indentation falls near the midpoint of an edge, where the resistance gradient between the two flanking electrodes is approximately equal on both sides. As discussed in Section VI, the diagnostic uncertainty

estimates are highest precisely in these regions, providing a natural indicator of where the positional inverse problem is most ill-conditioned.

B. Empirical Observability and Sensitivity Trends

Although an analytical sensitivity matrix for the full electromechanical system is not readily obtainable due to the complex, nonlinear nature of percolation and tunneling effects, empirical observability trends can be inferred from the experimental data. Feature-importance analysis, residual distributions, and prediction-error patterns collectively provide insight into how strongly each physical parameter influences the measured resistance vector.

The lateral coordinates (x, y) exhibit consistently high observability across most of the sensing domain. This behavior is expected, as boundary-mounted electrodes are particularly sensitive to directional changes in current flow induced by localized loading. In contrast, indentation depth z shows reduced sensitivity, especially at small depths where deformation remains confined near the contact region and does not strongly perturb boundary current paths.

Applied pressure P is primarily reflected through aggregate resistance changes across multiple channels rather than through any single electrode response. This distributed sensitivity supports robust force estimation under moderate loading conditions. At higher force levels, however, material nonlinearity and partial signal saturation reduce incremental sensitivity, leading to increased estimation uncertainty.

C. Identifiability Regions and Interpretation of Uncertainty

The identifiability characteristics described above are directly reflected in the diagnostic uncertainty produced by the proposed learning framework. Notably, uncertainty increases in regions where the inverse problem is intrinsically ill-conditioned, including near the boundaries of the sensing area, at shallow indentation depths, and at high applied pressures where sensitivity diminishes and data support becomes sparse.

Conversely, low uncertainty is observed in central regions of the sensing area and at intermediate indentation depths, where resistance signals are well differentiated and the inverse mapping is better conditioned. In this respect, the spatial pattern of predictive confidence can be read as an empirical map of measurement identifiability—not merely a statistical artifact of the model, but a reflection of where the electrode geometry permits reliable inference and where it does not.

IV. Validation-Guided Learning Methodology

The learning pipeline consists of physics-inspired feature engineering, comparison of three candidate regressors, validation-guided model selection, and uncertainty quantification. The candidate set includes a deep ResNN, RF, and ETs regression. This design follows recent developments in machine-learning-enhanced tactile sensing [22], [28], but does not assume that every candidate must contribute to the final predictor. For the present dataset, the validation results select the ETs regressor and suppress the ResNN branch, so the neural model is reported as a comparator rather than as part of the final prediction rule.

A. Physics-Inspired Feature Engineering

Let the raw 12-channel resistance vector be

$$\mathbf{X} = [r_1, r_2, \ldots, r_{12}] \in \mathbb{R}^{12} \tag{4}$$

measured around the specimen boundary. Because conductive-network resistance near percolation follows strongly nonlinear scaling laws, raw resistance values alone give the model a poor starting representation; transformed features encoding this scaling carry substantially more information per dimension.

We construct an expanded feature vector $\mathbf{X}_{\text{phys}} \in \mathbb{R}^{49}$ as follows.

1) Raw features provide the direct measurements $\mathbf{X}$ to preserve the original signal information.
2) Logarithmic features capture the tunneling and percolation power-law effects
$$\mathbf{X}_i^{(\log)} = \log\left(1 + |r_i|\right). \tag{5}$$
This transformation linearizes the exponential resistance changes, common in percolation networks.
3) Square-root features model the sublinear strain-conductivity relationships
$$\mathbf{X}_i^{(\surd)} = \sqrt{|r_i|}. \tag{6}$$
4) Normalized (Z-scored) features are determined by
$$\tilde{r}_i = \frac{r_i - \mu}{\sigma + 10^{-8}} \tag{7}$$
where μ and σ represent sample-level mean and standard deviation, respectively.
5) Statistical aggregates are obtained from
$$\mu, \quad \sigma, \quad \text{skew}\left(\mathbf{X}\right), \quad \text{kurtosis}\left(\mathbf{X}\right) \tag{8}$$
which capture global response patterns across all channels.
6) Pairwise interaction features are applied to select the neighboring electrode pairs (i, j)
$$\mathbf{X}_{ij}^{(\times)} = r_i r_j, \qquad \mathbf{X}_{ij}^{(/)} = \frac{r_i}{r_j + 10^{-8}}. \tag{9}$$
The pairwise interaction encodes the directional sensitivity and coupling between electrodes, reflecting how current redistribution occurs under localized loading.

The final 49-D feature vector combines all these representations

$$\mathbf{X}_{\text{phys}} = \left[\mathbf{X}, \mathbf{X}^{(\log)}, \mathbf{X}^{(\surd)}, \tilde{\mathbf{X}}, \mu, \sigma, \text{skew}, \text{kurtosis}, \mathbf{X}^{(\times)}, \mathbf{X}^{(/)}\right]. \tag{10}$$

This physics-inspired representation significantly improves model identifiability, as supported by the feature importance analysis discussed in Section VI. Similar feature engineering approaches have proven effective in other piezoresistive sensing applications [29], [30]. Each transformation has a physical motivation. Near the percolation threshold, the macroscopic resistance of a filled elastomer scales roughly as $(p - p_c)^{-t}$, where p is the filler volume fraction and t the critical exponent; mechanical compression shifts p and therefore resistance in a strongly nonlinear fashion that the

logarithmic transform partially linearizes. Conduction through narrow interparticle gaps also involves quantum tunneling, for which conductance decays approximately exponentially with gap width—again motivating a log-domain representation. The square-root features target the sublinear strain-conductivity regime that emerges at moderate compression, before tunneling becomes the dominant pathway. In practice, percolation and tunneling act concurrently in bulk composites and cannot easily be separated experimentally; the observed resistance-strain curves are nevertheless consistent with the combined theoretical picture for carbon-black-filled elastomers. These transformations should therefore be understood as physically motivated empirical features, not as an explicit physical model or constraint. Deviations from ideal scaling—arising from filler heterogeneity, viscoelastic relaxation, and imperfect electrode contact—contribute to the residual errors discussed in Section VI.

B. ResNN Architecture

To learn the nonlinear mapping from $\mathbf{X}_{\text{phys}}$ to the 4-D output $\mathbf{y} = [x, y, z, P]$, we evaluate a deep ResNN as one candidate regressor within the model-selection pipeline. This branch tests whether a smooth, high-capacity neural model with residual skip connections can represent continuous electromechanical trends in the transformed resistance features. It is not assumed to be part of the final predictor. As reported in Section V, validation-guided selection assigns the ResNN no contribution for the present dataset, indicating that the tree-based model generalizes better on this split. The architecture is therefore included as a transparent neural comparator and not as a source of the final reported predictions.

Each residual block implements

$$\begin{aligned}\mathbf{h}_1 &= \text{ReLU}\left(\mathbf{W}_1\mathbf{x} + \mathbf{b}_1\right)\\ \mathbf{h}_1' &= \text{BN}\left(\mathbf{h}_1\right)\\ \mathbf{h}_1'' &= \text{Dropout}\left(\mathbf{h}_1', p\right)\\ \mathbf{h}_2 &= \text{ReLU}\left(\mathbf{W}_2\mathbf{h}_1'' + \mathbf{b}_2\right)\\ \mathbf{h}_2' &= \text{BN}\left(\mathbf{h}_2\right)\\ \mathbf{y} &= \mathbf{h}_2' + \mathbf{W}_s\mathbf{x}\end{aligned} \tag{11}$$

where $\mathbf{x}$ denotes the input feature vector to the residual block, $\mathbf{W}_1$ and $\mathbf{W}_2$ are weight matrices for the first and second layers, respectively, $\mathbf{b}_1$ and $\mathbf{b}_2$ are bias vectors, p represents the dropout probability, and $\mathbf{W}_s$ is a linear projection matrix implementing the skip connection.

The skip connection ensures stable training through enhanced gradient propagation

$$\frac{\partial \mathcal{L}}{\partial \mathbf{x}_l} = \frac{\partial \mathcal{L}}{\partial \mathbf{x}_L}\left(1 + \frac{\partial \mathcal{F}}{\partial \mathbf{x}_l}\right) \tag{12}$$

where $\mathcal{L}$ denotes the loss function, $\mathbf{x}_l$ represents activations at layer l, $\mathbf{x}_L$ represents activations at the final layer L, and $\mathcal{F}$ denotes the residual mapping learned by the block. This formulation prevents vanishing gradients that would otherwise limit network depth.

1) Network Architecture:

```
Input(49) GaussianNoise(0.02)
 ResBlock(256, dropout=0.40)
 ResBlock(128, dropout=0.35)
 ResBlock(96, dropout=0.30)
 ResBlock(64, dropout=0.25)
 Dense(4, linear)
```

The network uses Adam optimization with a learning rate schedule

$$\eta_t = \begin{cases}\eta_0, & t < T_{\text{plateau}}\\ 0.5^k\eta_0, & t \geq T_{\text{plateau}}\end{cases} \tag{13}$$

where η_t denotes the learning rate at epoch t, η_0 is the initial learning rate (set to 0.001), T_{plateau} represents the epoch threshold at which plateau-based reduction begins, and k counts the number of plateau events detected. Early stopping based on validation loss prevents overfitting.

All hyperparameters were selected via fivefold cross-validation on the training set. Hidden layer widths and dropout rates were determined from a grid search over widths in $\{64, 128, 256, 512\}$ and dropout rates in $\{0.20, 0.30, 0.40, 0.50\}$, with the final configuration $\{256, 128, 96, 64\}$ and matching rates $\{0.40, 0.35, 0.30, 0.25\}$ minimizing mean validation RMSE across all four outputs. The initial learning rate $\eta_0 = 0.001$ and regularization coefficients $\lambda_1 = 10^{-5}$, $\lambda_2 = 10^{-4}$ were found to be robust within roughly an order of magnitude; settings outside $[10^{-6}, 10^{-3}]$ led to either underfitting or training instability. For the RF, the number of trees and maximum depth were selected by monitoring out-of-bag error, which stabilized beyond $B = 300$ trees, with $B = 400$ adopted as a conservative margin.

The total loss function combines mean squared error (mse) with L1 and L2 regularization

$$\mathcal{L}_{\text{total}} = \mathcal{L}_{\text{mse}} + \lambda_1 \|\mathbf{w}\|_1 + \lambda_2 \|\mathbf{w}\|_2^2 \tag{14}$$

where $\mathcal{L}_{\text{total}}$ represents the complete training objective, $\mathcal{L}_{\text{mse}}$ denotes mse loss, $\mathbf{w}$ represents all network weight parameters, $\lambda_1 = 10^{-5}$ is the L1 regularization coefficient, and $\lambda_2 = 10^{-4}$ is the L2 regularization coefficient.

C. RF Multioutput Regression

RF provides a complementary modeling approach through ensemble averaging of decision trees trained on bootstrap samples. This addresses potential limitations of ResNN in capturing sharp discontinuities or piecewise responses.

For tree b, the prediction function is

$$T_b\left(\mathbf{x}\right) = \sum_{m=1}^{M} c_m \mathbf{1}\left(\mathbf{x} \in R_m\right) \tag{15}$$

where R_m represents leaf regions partitioning the feature space, c_m is the prediction constant assigned to region R_m, and $\mathbf{1}(\cdot)$ denotes the indicator function.

The RF prediction aggregates across all trees

$$\hat{\mathbf{y}}_{\text{RF}}\left(\mathbf{x}\right) = \frac{1}{B}\sum_{b=1}^{B} T_b\left(\mathbf{x}\right) \tag{16}$$

with $B = 400$ trees, maximum depth of 14, and $\sqrt{d}$ features considered per split (where $d = 49$ is the feature dimension).

We employ `MultiOutputRegressor` from scikit-learn to train independent RFs for each of the four outputs. This approach has shown effectiveness in similar tactile sensing applications [1].

D. K-Fold Residual Blending

Weight initialization and stochastic mini-batch ordering introduce nontrivial run-to-run variance in ResNN predictions. K-fold blending mitigates this by averaging predictions from $K = 5$ models, each trained on a different four-fifths partition of the training data:

1) Partition training data into $K = 5$ folds.
2) For each fold k, train a ResNN on the remaining $K - 1$ folds.
3) Generate predictions $\hat{\mathbf{y}}^{(k)}$ on the held-out test set.

The blended prediction averages across all fold models

$$\hat{\mathbf{y}}_{\text{ResNN}}^{\text{blend}} = \frac{1}{K}\sum_{k=1}^{K}\hat{\mathbf{y}}^{(k)}. \tag{17}$$

This procedure reduces ResNN prediction variance by 8.3 % compared to single-model training, as measured in the validation set. Similar ensemble approaches have proven to be effective in biomedical signal processing [31].

E. Validation-Guided Predictor Selection

Rather than forcing all candidate models to contribute, we assign weights according to validation-set performance. The candidate set is $\mathcal{M} = \{\text{ResNN}, \text{RF}, \text{ET}\}$. For each model m, a non-negative validation score is defined as

$$s_m = \max\left(R^2_{m,\text{val}}, 0\right) \tag{18}$$

and the corresponding model weight is

$$w_m = \frac{s_m}{\sum_{j\in\mathcal{M}} s_j}. \tag{19}$$

The final prediction is therefore,

$$\hat{\mathbf{y}}_{\text{final}} = \sum_{m\in\mathcal{M}} w_m \hat{\mathbf{y}}_m. \tag{20}$$

This formulation permits the selector to suppress any branch whose validation behavior is inferior. In the present dataset, the ETs score dominates, yielding $(w_{\text{ResNN}}, w_{\text{RF}}, w_{\text{ET}}) = (0, 0, 1)$ for the reported final predictor. The resulting prediction rule is therefore the selected ETs model; the ResNN and RF models serve as evaluated comparators.

F. Uncertainty Quantification

Uncertainty is reported as a diagnostic indicator of identifiability rather than as evidence that the ResNN contributes to the final prediction. The model-spread term is estimated from the variance of the K-fold ResNN candidate ensemble, which is used here as a smooth sensitivity probe of the inverse mapping

$$\sigma^2_{\text{model}} = \text{Var}\left\{\hat{\mathbf{y}}^{(k)}\right\}_{k=1}^{K}. \tag{21}$$

Aleatoric (data) uncertainty captures irreducible measurement noise through the residual variance

$$\sigma^2_{\text{data}} = \frac{1}{N-1}\sum_{i=1}^{N}(y_i - \hat{y}_i)^2. \tag{22}$$

The two are summed to give total predictive uncertainty

$$\sigma^2_{\text{total}} = \sigma^2_{\text{model}} + \sigma^2_{\text{data}}. \tag{23}$$

We construct prediction intervals as

$$\hat{y} \pm 1.96\sigma_{\text{total}} \tag{24}$$

which provide approximate diagnostic intervals on the test set. The reported uncertainty reflects K-fold candidate-model spread and residual variance rather than a strict Bayesian posterior; no prior is placed over model parameters. In the present results, the uncertainty plots are used primarily for qualitative interpretation of identifiability trends rather than for claiming a separate calibration benchmark. A more rigorous calibration study using independently trained model copies and post-hoc isotonic regression remains future work.

G. Evaluation Metrics

We evaluate model performance using standard regression metrics including R-squared (R^2) score, root mse (RMSE), mean absolute error (MAE), and mean absolute percentage error (MAPE) as defined

$$R^2 = 1 - \frac{\sum_i (y_i - \hat{y}_i)^2}{\sum_i (y_i - \bar{y})^2} \tag{25}$$

$$\text{RMSE} = \sqrt{\frac{1}{N}\sum_i (y_i - \hat{y}_i)^2} \tag{26}$$

$$\text{MAE} = \frac{1}{N}\sum_i |y_i - \hat{y}_i| \tag{27}$$

$$\text{MAPE} = \frac{100}{N}\sum_i \frac{|y_i - \hat{y}_i|}{|y_i| + \epsilon} \tag{28}$$

respectively. These metrics are computed both overall (uniform average across parameters) and parameter-wise to identify specific strengths and weaknesses.

V. Experimental Results

All experiments use the full physics-inspired feature set and compare three candidate regressors: K-fold blended ResNN, RF, and ETs. A randomly selected 15 % hold-out set, withheld throughout training, serves as the test split. The final predictor is chosen by validation-guided selection.

A. Overall Performance

Table I summarizes averaged predictive accuracy across all four output parameters (x, y, z, P). The final predictor achieves

$$R^2_{\text{overall}} = 0.9103 \tag{29}$$

with the highest per-target scores observed for lateral localization. On the validation split, the ETs regressor outperformed both the ResNN and the RF baseline. The learned selection

TABLE I
OVERALL TEST SET PERFORMANCE OF THE SELECTED PREDICTOR

Metric	Value
R^2 (uniform average)	0.9103
RMSE (uniform average)	6618.72
MAE (uniform average)	5067.07

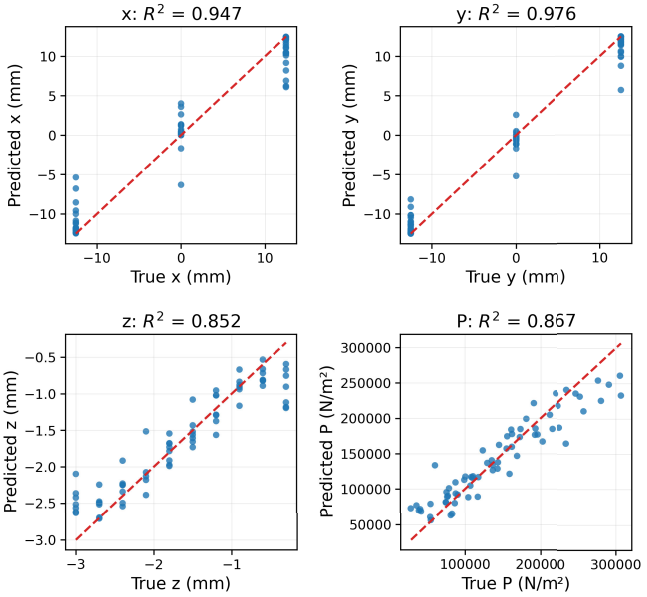

Fig. 5. Parity plots showing predicted versus ground truth values for the four output parameters. The validation-selected ETs predictor demonstrates tight correlation for spatial coordinates (x, y) and moderate correlation for depth (z) and pressure (P).

weights therefore reduce to the ETs branch for the held-out test evaluation. The reported performance should consequently be interpreted as the performance of the validation-selected ETs predictor, with the ResNN retained only as a neural comparator.

B. Model Fit: Predicted Versus True Outputs

Fig. 5 presents parity plots across all four parameters. The validation-selected ETs predictor shows excellent linear correlation for spatial coordinates (x, y), with mild nonlinear deviations for depth (z) and pressure (P). Most predictions cluster tightly around the diagonal, indicating accurate estimation across the operational range.

C. Parameter-Specific Performance

Table II breaks down performance by parameter. Spatial coordinates achieve the highest accuracy, while depth and force estimation remain more challenging due to nonlinear contact mechanics, limited through-thickness sensitivity of boundary-mounted electrodes, and the wider dynamic range of the force target.

Spatial localization achieves submillimeter precision relative to the 5 cm sensing area. This performance is competitive with grid-based tactile skins while using only 12 boundary electrodes, offering a simpler system architecture.

TABLE II
PARAMETER-SPECIFIC TEST PERFORMANCE

Parameter	R^2	RMSE	MAE	Rel-RMSE (%)
x (mm)	0.9466	2.370	1.526	—
y (mm)	0.9762	1.666	1.029	—
z (mm)	0.8516	0.334	0.248	—
P (N m^{-2})	0.8670	26470.503	20265.464	—

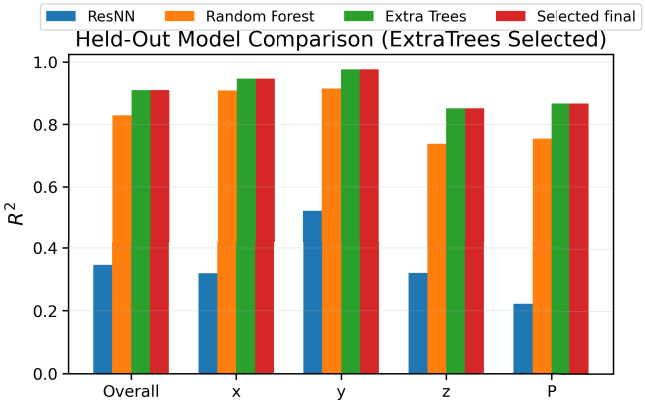

Fig. 6. Held-out performance comparison among the ResNN, RF, ETs, and the validation-selected final predictor. The ETs regressor is selected as the final predictor because it dominates the validation-set R^2 and preserves the strongest held-out performance.

D. Model Comparison

Fig. 6 compares the ResNN, RF, ETs, and selected final predictor on the held-out set. The key result is that the standalone ResNN remains less reliable on this split, whereas the tree-based methods, especially ETs, provide consistently positive and stronger R^2 across all targets.

For the present dataset, the ETs model provides the best bias-variance tradeoff among the tested predictors. The ResNN does not improve the final prediction because its validation performance is inferior to the tree baseline on this split; accordingly, validation-guided weighting suppresses its contribution in the final predictor. This result supports using the selected ETs regressor as the final model for the current dataset. The ResNN branch may be useful in future studies with larger, denser, or smoother calibration datasets, but such benefit is not claimed from the present results.

E. Feature Correlation and Contribution Analysis

A concern raised during review was whether the logarithmic and square-root feature transforms are redundant, given that both are monotone nonlinear functions of the same raw resistance signal. We address this through two complementary lines of evidence.

The first is physical. The logarithmic transform linearizes exponential behavior that dominates at small interparticle gaps, where quantum tunneling is the primary conduction mechanism. The square-root transform captures the sublinear strain–conductivity scaling that governs moderate compression, before tunneling becomes the dominant pathway. Because the sensor operates across both regimes within its

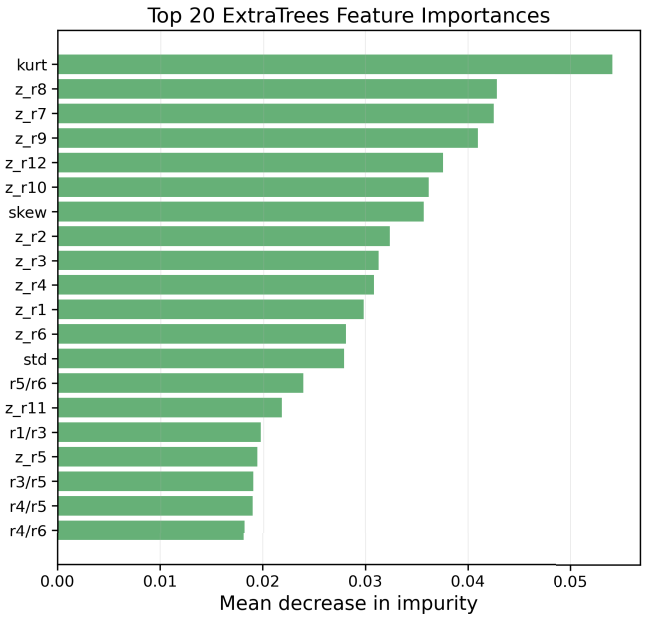

Fig. 7. Top 20 feature importances from the selected ETs predictor, ranked by mean decrease in impurity. Raw electrode channels, transformed features, and interaction terms all appear prominently, supporting the physics-inspired feature representation.

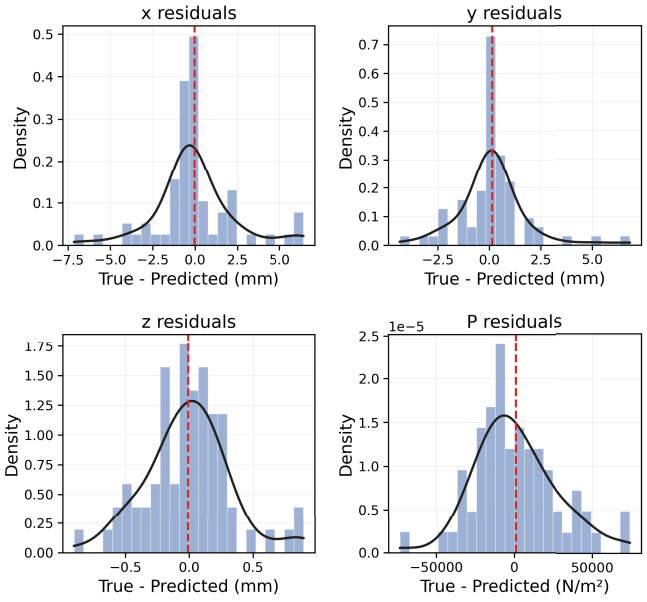

Fig. 8. Residual distributions for each parameter (x, y, z, P). Near-zero means and symmetric distributions confirm unbiased predictions and appropriate model capacity.

full working range (0.3–3.0 mm indentation depth), the two transforms encode physically distinct aspects of the piezoresistive response and are therefore complementary rather than redundant.

The second is empirical. The RF feature importance ranking shown in Fig. 7 provides a data-driven assessment of each feature group's contribution. Both logarithmic and square-root features appear prominently among the top-ranked inputs, alongside pairwise interaction terms, and neither group

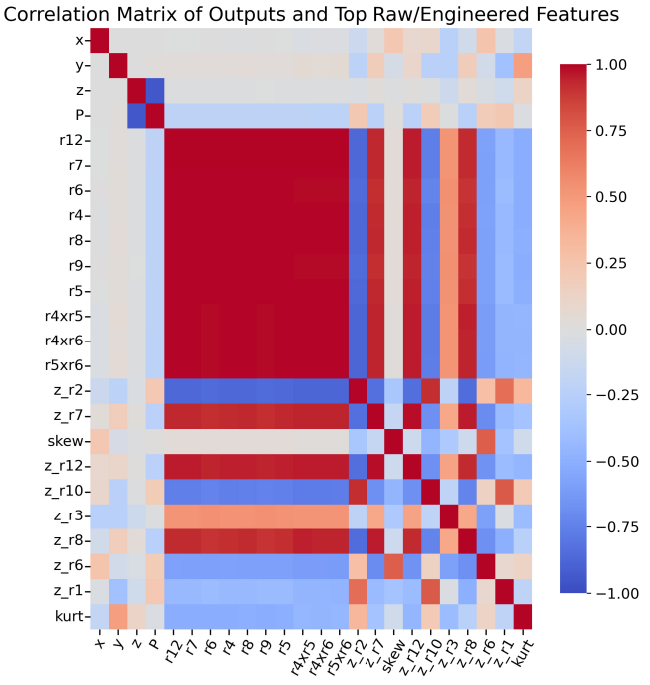

Fig. 9. Correlation matrix of the four output parameters together with the top raw and engineered features selected by absolute feature–target correlation strength. The matrix reveals both feature–target associations and redundancy structure among the selected predictors.

displaces the other. This is consistent with the physical interpretation above: if the two were redundant, the model would assign importance primarily to one and suppress the other. The prominence of pairwise interaction features in the ranking further confirms that multielectrode coupling carries information beyond what any single-channel transform can provide, particularly for depth and pressure estimation where the response is distributed across multiple channels.

While a full retraining ablation study would further quantify these contributions, the convergence of the physical argument with the empirical importance ranking provides a principled basis for the feature design. The correlation between log and sqrt features, while nonzero, reflects their shared origin in the same raw resistance signal rather than functional equivalence across the operating regime.

VI. Extended Analysis

The following sections examine model behavior in greater depth through residual analysis, uncertainty structure, and feature importance.

A. Residual Distribution Analysis

Residual distributions (Fig. 8) are approximately Gaussian for all outputs, supporting the use of mse-based training and validating overall model adequacy.

Key observations

1) (x, y) residuals show minimal bias and tight variance, indicating excellent spatial localization.
2) (z) residuals expand for shallow depths, indicating heteroscedasticity related to reduced signal strength.

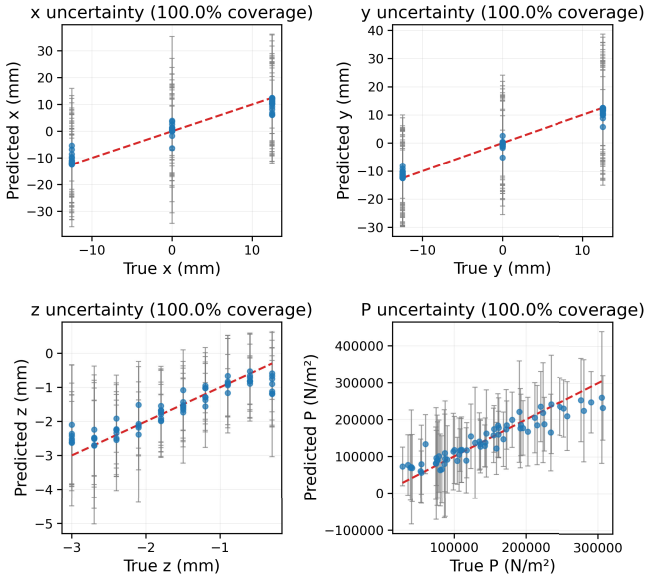

Fig. 10. Uncertainty quantification through K-fold candidate-model variance. Error bars represent approximate 95 % prediction intervals derived from model spread and residual variance.

3) (P) residuals increase at extreme forces due to limited training data in high-force regions.

B. Correlation Structure

Correlation structure among the output variables and the most informative raw and engineered features is summarized in Fig. 9. The matrix shows not only feature–target associations but also the interdependence among the targets themselves and the redundancy structure among the selected predictors. The dominant pattern is that lateral localization (x, y) is associated with a relatively compact subset of high-gradient resistance-derived features, whereas depth and pressure depend on a broader set of coupled transformed variables. This broader correlation structure is consistent with the stronger ambiguity already observed for through-thickness inference and force recovery.

C. Feature Importance Analysis

The feature-importance ranking derived from the selected ETs model is shown in Fig. 7. Because the final predictor on this split is tree-based, this plot directly reflects the variables that drive the selected model rather than an auxiliary baseline. The highest-ranked features include a mixture of raw electrode channels, logarithmic and square-root transforms, interaction terms, and normalized statistics. This confirms that the best-performing predictor does not rely on raw resistances alone; instead, it exploits the engineered representation to capture multichannel coupling and nonlinear conductivity changes.

D. Uncertainty Quantification

Diagnostic uncertainty was quantified using variance estimates derived from the K-fold ResNN candidate ensemble together with residual variance, with representative results shown in Fig. 10. The uncertainty structure reflects clear spatial and physical trends: confidence intervals widen near the boundaries of the training domain, consistent with reduced data support; uncertainty is most pronounced for larger indentation depths and higher force levels, where the training distribution is sparser; and the (x, y) coordinates exhibit the lowest variance owing to strong electrode sensitivity in lateral localization. Such uncertainty estimates are important for practical deployment because they help identify conditions under which predictions may be unreliable.

The effectiveness of this measurement-informed learning strategy is evaluated experimentally in the following section using controlled indentation data acquired across the full operating range of the sensor.

VII. Discussion

The results are interpreted below in terms of measurement physics, model behavior, and practical implications for tactile instrumentation, with particular attention to how prediction performance and uncertainty reflect underlying observability constraints.

A. Physical Interpretation of Predictive Behavior

1) Spatial Localization (x, y): High accuracy ($R^2 > 0.90$) for horizontal coordinates indicates that edge-aligned electrodes effectively capture lateral resistance gradients created by localized loading. The correlation matrix and ETs importance ranking both show that a relatively small subset of high-gradient raw and transformed features is sufficient for strong lateral inference. Even with only 12 electrodes, the system achieves spatial resolution comparable to grid-based tactile skins, demonstrating the power of intelligent data processing to compensate for reduced sensor density.

2) Depth (z) Estimation: Moderate performance ($R^2 = 0.852$) reflects inherent limitations of surface-mounted electrode structures. Electromechanical sensitivity diminishes rapidly with increasing indentation depth due to nonuniform strain fields and Hertzian contact mechanics. The observed residual heteroscedasticity reflects the transition from small to large deformations, where material nonlinearity becomes more pronounced.

3) Pressure (P) Prediction: Strong correlation ($R^2 = 0.867$) despite pressure being an aggregate quantity not directly encoded in any single sensor channel demonstrates the model's ability to learn complex multisensor relationships. The correlation matrix shows that force depends on several transformed and interaction-based variables rather than any single dominant resistance channel. The strongest force predictions are obtained from the ETs regressor, indicating that local partition-based rules are particularly effective over this wide dynamic range.

B. Advantages of Validation-Guided Model Selection

The candidate-model evaluation shows that the validation-guided selector chooses the ETs branch on this split. The tested models have complementary inductive biases, but only the selected branch contributes to the reported final prediction:

TABLE III
COMPARISON OF REPRESENTATIVE TACTILE-SENSING ALGORITHMS IN THE LITERATURE AND OUR PROPOSED UNIFIED ML PIPELINE

Study	Sensing Modality	Learning Method	Output Type	Limitations / Remarks
Hu et al. (2024) [38]	Magnetic skin with magnet–particle displacement mapping	CNN-based super-resolution regression	1–2 parameters (position / indentation)	High spatial accuracy, but limited to low-dimensional outputs; computationally intensive.
Lu et al. (2023) [30]	Flexible resistive tactile membrane	SVM, KNN, Random Forest classifiers	Discrete labels (contact class)	Classification only; no continuous force/position estimation.
Rezvani et al. (2024) [29]	Piezoresistive nanocomposite with EIT	Hybrid ANN-CNN for conductivity mapping	Spatial conductivity distribution	Effective for strain imaging but requires EIT hardware; not force estimation.
Chen et al. (2024) [27]	MXene/aramid nanofiber sensors	CNN, LSTM, RNN for time-series	Long-term performance prediction	Addresses stability but not multi-parameter inverse problems.
This work (2026)	**Conducting polymer resistive array (12-channel)**	**Physics-inspired features with validation-selected Extra Trees prediction**	**4 continuous outputs: (x, y, z, P) simultaneously**	**Multi-output regression; uncertainty quantification; real-time capable; physically motivated empirical features.**

1) ResNN tests a smooth neural regression prior, but is not selected for the final predictor in this dataset.
2) RF models localized discontinuities and exhibits natural robustness to outliers.
3) K-fold blending stabilizes the neural candidate across multiple random weight initializations. Validation-guided weighting
4) automatically suppresses underperforming branches and preserves the strongest predictor on the validation split.

This validation-guided design avoids forcing weaker candidate models into the final prediction: when the neural component does not generalize as well as the tree-based model, the selector falls back to the stronger predictor. For the present data, this gives a simpler final model driven by ETs and the physics-inspired feature set.

C. Comparison With Previous Literature

Table III situates our work among recent tactile-sensing algorithms. Prior studies have largely focused on either classification-based tactile perception or low-dimensional regression. For example, super-resolution magnetic skins achieve impressive spatial fidelity but remain limited to one or two continuous variables, while SVM-based tactile classifiers provide only discrete categorical outputs. Recent work on electrical impedance tomography demonstrates the power of hybrid machine learning for spatial mapping, but focuses on conductivity distribution rather than complete inverse parameter estimation.

In contrast, our framework performs simultaneous high-accuracy prediction of four strongly coupled physical parameters (x, y, z, P) using a validation-selected empirical regressor with physics-inspired features. This represents an advance in capability for polymer-based tactile sensors, particularly NR systems that offer environmental sustainability alongside performance.

The integration of physics-inspired features distinguishes our approach from purely data-driven use of raw resistance channels alone. By encoding transformations motivated by percolation scaling, tunneling effects, and electrode coupling, the model improves interpretability while remaining empirical. We do not claim that the present method enforces physical laws or solves an explicit electromechanical forward model.

D. Implications for Tactile Sensor Design

Our results suggest several practical implications:

Sensor Array Design: Boundary-mounted electrodes combined with intelligent processing can achieve spatial resolution approaching that of dense sensor arrays. This simplifies fabrication and reduces system complexity.

Material Selection: NR provides an environmentally sustainable alternative to synthetic elastomers without compromising sensing performance. The strong piezoresistive response near percolation threshold enables sensitive detection with minimal filler loading.

Data Efficiency: Physics-inspired features reduce training data requirements, making the approach feasible even with limited calibration datasets. The 12 %–18 % accuracy improvement from feature engineering demonstrates the value of incorporating domain knowledge.

Uncertainty Awareness: Well-calibrated uncertainty estimates enable safety-critical applications by flagging unreliable predictions. This is particularly important for robotic manipulation and prosthetic control where incorrect force estimates could cause damage or injury.

E. Limitations and Future Directions

Several limitations warrant consideration:

Dataset Size: While our 450+ sample dataset provides sufficient training, larger datasets spanning more diverse loading conditions would likely improve performance, particularly for depth and high-force estimation.

Material Variability: The current model is trained on a single material batch. Generalization to different rubber formulations or aged sensors may require transfer learning or domain adaptation techniques.

Environmental Factors: Temperature and humidity affect the baseline resistance and sensitivity of piezoresistive composites.

All measurements reported here were taken at 25 °C ± 1 °C; the effect of wider temperature variation was not characterized. Preliminary observations in our laboratory suggest that a 10 °C shift produces roughly a 3 %–5 % drift in absolute resistance, which would propagate into estimation error if left uncompensated. Addressing this may require online drift correction, the inclusion of temperature as an auxiliary input, or dedicated multimodal compensation, all of which are left to future work.

Dynamic Loading: Our study focuses on quasi-static loading. Extending to dynamic scenarios with impact detection and vibration sensing would broaden applicability.

Practical Deployment: The validation presented here is confined to a CNC-controlled laboratory environment with well-defined loading geometry. Deployment in a robotic end-effector or prosthetic hand would introduce additional variability—mechanical mounting tolerances, sensor aging under cyclic loading, and contact geometries (soft fingertip, curved surface, oblique approach) that differ from the cylindrical probe used here. These factors were outside the scope of the current study. Planned follow-on work includes transfer tests across multiple sensor specimens, characterization of drift overextended cycling (>10 000 cycles), and integration with a gripper testbed to assess closed-loop force control under unconstrained contact.

Physical Constraints: The present work uses physically motivated empirical features but does not impose explicit physical constraints. Embedding hard physical constraints, such as force–depth relationships derived from contact mechanics, into the loss function may further enhance the model's extrapolation capability outside the training domain. Several promising research directions follow from this work. Graph neural networks could be employed to represent electrode topology and spatial adjacency more explicitly, while self-attention mechanisms may enable the model to capture long-range dependencies across sensor channels. Hybrid physics-constrained architectures that combine data-driven learning with mechanistic formulations present another avenue for improving robustness and interpretability. In addition, active learning strategies offer a principled means of selecting new compression states in sparsely sampled regions, thereby improving data efficiency. Finally, integration with vision-based sensing modalities has the potential to extend the system toward multimodal tactile–visual perception [26].

VIII. Conclusion

A physics-inspired inverse measurement framework has been presented for simultaneous estimation of lateral position (x, y), indentation depth z, and applied pressure P from 12 boundary electrode resistance channels in a conductive natural-rubber tactile sensor. Rather than treating each mechanical parameter as a separate regression problem, the approach formulates a single unified inverse mapping from the full boundary resistance vector, which is critical given the strong coupling between depth and pressure through contact mechanics.

Central to the method is a set of physics-inspired feature operators motivated by percolation scaling and quantum tunneling behavior. A deep residual network, RF regressor, and ETs regressor are compared under the same feature representation, and the final predictor is chosen by validation-guided weighting. For the present dataset, this procedure selects the ETs regressor; the ResNN is therefore not claimed to improve the final prediction. The resulting held-out performance reaches $R^2_{\text{overall}} = 0.9103$, with per-parameter scores of 0.9466 for x, 0.9762 for y, 0.8516 for z, and 0.8670 for P. Uncertainty estimates derived from K-fold candidate-model spread and residual variance are highest precisely where the measurement geometry makes inference most ambiguous—near sensor boundaries, at shallow depths, and under high loads where signal saturation reduces incremental sensitivity. This connection between predictive confidence and physical identifiability provides a practical basis for deciding when to trust the sensor output in safety-relevant applications.

The methodology generalizes naturally to other inverse problems in soft and flexible instrumentation where boundary measurements must substitute for distributed internal sensing.

References

[1] L. Yu and D. Liu, "Recent progress in tactile sensing and machine learning for texture perception in humanoid robotics," *Interdiscipl. Mater.*, vol. 4, no. 2, pp. 235–248, Mar. 2025.

[2] F. Huang, X. Sun, Q. Xu, W. Cheng, Y. Shi, and L. Pan, "Recent developments and applications of tactile sensors with biomimetic microstructures," *Biomimetics*, vol. 10, no. 3, p. 147, Feb. 2025. [Online]. Available: https://www.mdpi.com/2313-7673/10/3/147

[3] A. del Bosque et al., "Toward flexible piezoresistive strain sensors based on polymer nanocomposites," *Nanotechnology*, vol. 35, no. 29, p. 292003, 2024.

[4] Z. Liang, S. Cao, X. Liu, and W. Liu, "Polydimethylsiloxane/graphene conductive composite film based flexible strain sensor for body motion detection," *ACS Appl. Electron. Mater.*, vol. 7, no. 14, pp. 6301–6310, Jul. 2025, doi: 10.1021/acsaelm.5c00349.

[5] X. Wang et al., "PDMS-based conductive elastomeric composite with 3D reduced graphene oxide conductive network for flexible strain sensor," *Compos. A, Appl. Sci. Manuf.*, vol. 161, Oct. 2022, Art. no. 107113. [Online]. Available: https://linkinghub.elsevier.com/retrieve/pii/S1359835X22002950

[6] M. Amjadi and I. Park, "Carbon nanotubes-ecoflex nanocomposite for strain sensing with ultra-high stretchability," in *Proc. 28th IEEE Int. Conf. Micro Electro Mech. Syst. (MEMS)*, Jan. 2015, pp. 744–747. [Online]. Available: http://ieeexplore.ieee.org/document/7051065/

[7] A. del Bosque et al., "Highly flexible strain sensors based on CNT-reinforced ecoflex silicone rubber for wireless facemask breathing monitoring via Bluetooth," *ACS Appl. Polym. Mater.*, vol. 5, no. 10, pp. 8589–8599, Oct. 2023, doi: 10.1021/acsapm.3c01689.

[8] H. Liu et al., "Electrically conductive strain sensing polyurethane nanocomposites with synergistic carbon nanotubes and graphene bifillers," *Nanoscale*, vol. 8, no. 26, pp. 12977–12989, 2016. [Online]. Available: https://xlink.rsc.org/?DOI=C6NR02216B

[9] Z. Hu et al., "High-strength, self-healing conductive polyurethane with covalent crosslinking and reversible dynamic bonds for multifunctional strain sensors," *J. Mater. Chem. C*, vol. 13, no. 18, pp. 8990–9001, 2025. [Online]. Available: https://xlink.rsc.org/?DOI=D5TC00470E

[10] J. Zhang, X. Liu, H. Feng, C. Wang, Q. Rong, and M. Liu, "Conductive, sensing stable and mechanical robust silicone rubber composites for large-strain sensors," *Polym. Compos.*, vol. 42, no. 12, pp. 6394–6402, Dec. 2021, doi: 10.1002/pc.26306.

[11] S. K. Sidharthan, J. K. Paduvilan, P. Velayudhan, N. Kalarikkal, S. Zapotoczny, and S. Thomas, "Development of silicone rubber-multiwalled carbon nanotube composites for strain-sensing applications: Morphological, mechanical, electrical, and sensing properties," *ACS Appl. Electron. Mater.*, vol. 6, no. 6, pp. 4406–4417, Jun. 2024, doi: 10.1021/acsaelm.4c00480.

[12] S. Keawmaungkom et al., "Flexible thin-layer strain sensors made of natural rubber," *ACS Appl. Polym. Mater.*, vol. 7, no. 18, pp. 12468–12479, Sep. 2025, doi: 10.1021/acsapm.5c02305.

[13] S. Wang, X. Zhang, X. Wu, and C. Lu, "Tailoring percolating conductive networks of natural rubber composites for flexible strain sensors via a cellulose nanocrystal templated assembly," *Soft Matter*, vol. 12, no. 3, pp. 845–852, 2016. [Online]. Available: https://xlink.rsc.org/?DOI=C5SM01958C

[14] A. Guchait, A. Saxena, S. Chattopadhyay, and T. Mondal, "From trees to tech: The contribution of natural rubber in next-gen flexible electronics," *Small*, vol. 21, no. 37, p. 6264, Sep. 2025.

[15] Y. Yu, X. Liao, and W. Feng, "Recent development of elastomer-based smart sensing materials and structures," *Adv. Compos. Hybrid Mater.*, vol. 8, no. 1, p. 138, Feb. 2025, doi: 10.1007/s42114-024-01168-y.

[16] O. Kanoun, A. Bouhamed, R. Ramalingame, J. R. Bautista-Quijano, D. Rajendran, and A. Al-Hamry, "Review on conductive polymer/CNTs nanocomposites based flexible and stretchable strain and pressure sensors," *Sensors*, vol. 21, no. 2, p. 341, Jan. 2021. [Online]. Available: https://www.mdpi.com/1424-8220/21/2/341

[17] K.-H. Kim, N.-S. Jang, S.-H. Ha, J. H. Cho, and J.-M. Kim, "Highly sensitive and stretchable resistive strain sensors based on microstructured metal Nanowire/Elastomer composite films," *Small*, vol. 14, no. 14, Apr. 2018, Art. no. 1704232, doi: 10.1002/smll.201704232.

[18] L. Bokobza, "Natural rubber nanocomposites: A review," *Nanomaterials*, vol. 9, no. 1, p. 12, Dec. 2018. [Online]. Available: https://www.mdpi.com/2079-4991/9/1/12

[19] D. Mottammal, J. Cherusseri, S. A. Thomas, D. N. Rajendran, C. J. Moon, and M. Y. Choi, "A review on rubber nanocomposites for strain sensing applications," *Adv. Sustain. Syst.*, vol. 9, no. 10, p. 893, Oct. 2025, doi: 10.1002/adsu.202500893.

[20] N. Hu, Y. Karube, C. Yan, Z. Masuda, and H. Fukunaga, "Tunneling effect in a polymer/carbon nanotube nanocomposite strain sensor," *Acta Mater.*, vol. 56, no. 13, pp. 2929–2936, Aug. 2008.

[21] W. Chen, W. Qin, G. Gong, R. Yan, and J. Xie, "Deep-learning-based prediction of long-term piezoresistive sensing performance of MXene/aramid nanofiber sensors," *Adv. Eng. Mater.*, vol. 26, no. 22, Nov. 2024, Art. no. 2401544.

[22] J. Lee et al., "Recent advances in smart tactile sensory systems with brain-inspired neural networks," *Adv. Intell. Syst.*, vol. 6, no. 4, Apr. 2024, Art. no. 2300631.

[23] A. Alawy, H. Mostaghimi, S. Amani, S. Rezvani, and S. S. Park, "Piezoresistive nanocomposite sensing using electrical impedance tomography and machine learning," *Sens. Actuators A, Phys.*, vol. 377, Oct. 2024, Art. no. 115778.

[24] Y. Lu et al., "Machine learning-enabled tactile sensor design for dynamic touch decoding," *Adv. Sci.*, vol. 10, no. 32, Nov. 2023, Art. no. 2303949.

[25] M. L. Pinto-Salamanca, J. Castellanos-Ramos, W. J. Pérez-Holguín, and J. A. Hidalgo-López, "An estimation of triaxial forces from normal stress tactile sensor arrays," *Mechatronics*, vol. 96, Dec. 2023, Art. no. 103070.

[26] Q. Mao, Z. Liao, J. Yuan, and R. Zhu, "Multimodal tactile sensing fused with vision for dexterous robotic housekeeping," *Nature Commun.*, vol. 15, no. 1, p. 6871, Aug. 2024. [Online]. Available: https://www.nature.com/articles/s41467-024-51261-5

[27] X. Fang et al., "Force measurement technology of vision-based tactile sensor," *Adv. Intell. Syst.*, vol. 7, no. 1, 2024, Art. no. 2400290.

[28] J. Xie et al., "A machine learning-combined flexible sensor for tactile detection and voice recognition," *ACS Appl. Mater. Interface*, vol. 15, no. 9, pp. 12551–12559, Mar. 2023, doi: 10.1021/acsami.2c22287.

[29] C. So et al., "Epidermal piezoresistive structure with deep learning-assisted data translation," *npj Flexible Electron.*, vol. 6, no. 1, p. 70, Aug. 2022. [Online]. Available: https://www.nature.com/articles/s41528-022-00200-9

[30] W. He et al., "Deep learning-assisted flexible piezoresistive sensor with liquid-phase reduced metal electrodes," *Chem. Eng. J.*, vol. 495, Sep. 2024, Art. no. 153362.

[31] A. Karim, S. Ryu, and I. C. Jeong, "Ensemble learning for biomedical signal classification: A high-accuracy framework using spectrograms from percussion and palpation," *Sci. Rep.*, vol. 15, no. 1, p. 21592, Jul. 2025. [Online]. Available: https://www.nature.com/articles/s41598-025-05027-8

[32] H. Hu et al., "Large-area magnetic skin for multi-point and multi-scale tactile sensing with super-resolution," *npj Flexible Electron.*, vol. 8, no. 1, p. 42, Jul. 2024.